Supporting information for:

An allosteric palindromic hairpin probe based dual-mode interactive strand displacement amplification enables robust miRNA biosensing

Experimental section

Materials and reagents

The Klenow Fragment (3'-5' exo-, 5 U/μL) was utilized in conjunction with 10× NEBuffer 2 (500 mM NaCl, 100 mM $MgCl_2$, 100 mM Tris-HCl, 10 mM DTT, pH 7.9). The Nt.BbvCI endonuclease (10 U/μL) was employed alongside 10× Cutsmart buffer (200 mM Tris-acetate, 100 mM magnesium acetate, 500 mM potassium acetate, pH 7.9), supplemented with BSA at a concentration of 1 mg/mL. Both the Klenow Fragment and Nt.BbvCI endonuclease reagents were sourced from New England Biolabs Co., Ltd. (Beijing, China). The tris-buffer (10 mM Tris-HCl, 100 mM NaCl, 10 mM $MgCl_2$, pH 8.2), 1× TBE electrophoresis buffer (90 mM Tris, 90 mM boric acid, 10 mM EDTA, and 7 M urea, pH 8.0), a solution of acrylamide and bis-acrylamide in a ratio of 29:1 (30%), N,N,N',N'-Tetramethylethylenediamine (TEMED), ammonium persulfate (AP), 10000× SYBR Green I, deoxynucleotide triphosphates (dNTPs) at a concentration of 10 mM, and 10×DNA loading buffer were provided by Servicebio Biotechnology Co., Ltd. (Wuhan, China). The serum miRNA extraction kit was supplied by HaiGene Biotechnology Co., Ltd. (Harbin, China). The PrimeScript RT reagent kit and Premix Ex Taq were obtained from Takara Biomedical Technology Co., Ltd. (Beijing, China). Oligonucleotides (**Table S1**) and ThT were acquired from Sangon Biotech Co. Ltd. (Shanghai, China). Oligonucleotides were purified using high-performance liquid chromatography and dissolved in 1× TE buffer to prepare storage solutions at a concentration of 10 μM. Ultrapure water with a resistance

of 18.2 MΩ, generated from a Milli-Q Water Purification System (Millipore, USA), was utilized in this study.

Instruments

Fluorescence measurements were carried out using a PerkinElmer FL8500 Fluorescence Spectrophotometer (Waltham, USA) with specific parameters set as follows: an excitation wavelength of 430 nm, a slit width of 10/10 nm, a scanning speed of 1200 nm/min, a recording range from 450 to 600 nm, and the PMT detector voltage set at 650 V. Electrophoresis analysis was conducted using a Servicebio PW-600 electrophoresis analyzer (Wuhan, China), and the gel image was captured using a ChampGel 7000 gel imaging system (Beijing, China). Quantitative reverse transcription-polymerase chain reaction (qRT-PCR) reactions were run in triplicates on a Bio-Rad CFX Connect Real-Time PCR System (California, USA). The reaction temperature was consistently regulated using a Bio-Rad T100 thermal cycler system (Hercules, USA). Circular dichroism (CD) measurements were conducted using a JASCO J-1700 CD spectrometer (Tokyo, Japan) at room temperature. The procedure involved accumulating and averaging three scans under the following parameters: a wavelength range from 200 to 500 nm, a scanning speed of 200 nm/min, a response time of 0.5 s, a bandwidth of 1.0 nm, and a quartz cuvette with a 0.1 cm path length. For sample preparation, 10 μM G-rich oligomers were added to Tris-buffer (25 mM, pH 7.4, 50 mM KCl) and incubated at room temperature for several hours.

DMI-SDA Based miRNA-155 Assay

Before detection, the APHP underwent annealing at 95 °C for 5 min, followed by a gradual cooling to room temperature to stabilize its hairpin structure. Subsequently, a mixture comprising 6 μL ddH_2O, 2 μL APHP (5 μM), and 2 μL target miRNA-155 at a specific concentration was combined and incubated at 37 °C for 10 min. The reaction mixture was then sequentially supplemented with 1 μL

Klenow fragment (5 U/μL), 1 μL Nt.BbvCI endonuclease (10 U/μL), 1 μL dNTPs (10 mM), 2 μL NEBuffer 2 (10×), 2 μL Cutsmart (10×), and finally with an additional 2 μL ddH_2O. After a further incubation at 37 °C for 1 h, followed by annealing at 60 °C for an additional 10 min to terminate enzyme activities, the resulting 20 μL sample was subsequently thoroughly mixed with 160 μL ddH_2O and 20 μL of Tris buffer (250 mM, pH = 7.4) containing 1 M NaCl and 10 μM ThT. Following a 1 h reaction at 37 °C, the aforementioned solution was transferred to a microcuvette for subsequent fluorescence recording, and the peak fluorescent signal at 493 nm was recorded. It is noteworthy that the final concentrations of all oligonucleotide species, including APHP, were determined based on the resulting total volume of the solution, which equaled 200 μL.

Signal Preservation Demonstration

To demonstrate the signal preservation ability of mono-G-triplex in combination with ThT. Firstly, 2.5 μL of 10 μM mono-G-triplex was mixed with 5 μL of 10 μM complementary mono-G-triplex (C-mono-G-triplex) at 37 °C for 10 min. Then, 172.5 μL ddH_2O and 20 μL of ThT (10 μM) was introduced to bind with the G-triplex motif at 37 °C for 30 min. For control purposes, an equivalent volume and concentration of either mono-G-triplex or C-mono-G-triplex were employed as controls. Similarly, to classify the signal preservation ability of the dimer-G-triplex, the procedures were replicated with the only difference being the substitution of mono-G-triplex with dimer-G-triplex and C-mono-G-triplex with C-dimer-G-triplex, respectively.

Polyacrylamide Gel Electrophoresis (PAGE) Analysis

The 12% native-PAGE gel was freshly prepared by mixing 5.9 mL of ddH_2O, 6 mL of 30% acrylamide: bis-acrylamide, 3 mL of 10× TBE buffer, 110 μL of 10% AP, and 10 μL of TEMED at room temperature for approximately 30 minutes. Subsequently, each sample well was loaded with a

mixture consisting of 8 μL of tested samples pre-mixed with 1 μL of 10× DNA loading buffer and 1 μL of 100× SYBR Green I. After electrophoresis in a TBE buffer solution (1×) at a voltage setting of 80 V for a duration of 90 minutes, the final gel image was captured using a gel imaging system.

Extraction of Total RNA from Blood

The human serum was obtained by centrifuging blood samples, kindly provided by the Fuyang People's Hospital, at 8,000 rpm for 15 min. Total RNAs were extracted from the serum using a serum miRNA extraction kit following the manufacturer's instructions. At first, 800 μL of serum miRNA reagent was mixed with 300 μL of human serum and incubated at room temperature for 5 min. After centrifugation at 13,000 rpm for 5 min, the supernatant was collected and combined with 1 mL of isopropanol. The resulting mixture underwent processing using a miRNA adsorption column through centrifugation at 13,000 rpm for 15 s. The extracted total miRNAs on the column were sequentially washed with 75% isopropanol and anhydrous ethanol through centrifugation at 13,000 rpm for each wash lasting 15 s. The filtrate was discarded. Finally, RNase-free H_2O was used to elute the absorbed miRNAs from the column after complete evaporation of residual ethanol occurred. Extracted total miRNAs were quantitated using a Thermo Fisher Scientific NanoDrop™ Spectrophotometer (Vantaa, Finland) at a wavelength of 260 nm and immediately utilized for cDNA synthesis in reverse transcription reactions.

Quantitative Real-time PCR (qRT-PCR) Analysis of miRNA-155

Prior to conducting qRT-PCR, reverse transcription reactions were performed in a 10 μL reaction mixture. The mixture consisted of 2 μL of PrimeScript (5×), 0.5 μL of PrimeScript RT Enzyme Mix I, 0.5 μL of a 50 μM stem-loop reverse transcription primer for miRNA-155, 2 μL of a 100 μM short linear reverse transcription primer for U6, and finally, it was supplemented with 1 μL diluted total

RNA (400 ng/μL) and 4 μL of RNase-free H_2O. The aforementioned steps were conducted under ice-cold conditions, and the resulting reaction solution was incubated at 37 °C for 15 min to facilitate completion of the reverse transcription reaction. Subsequently, the product was subjected to a brief incubation at 85℃ for 5 seconds in order to deactivate the reverse transcriptase, and the synthesized cDNA was stored at −80 ℃ for subsequent experiments. To perform qRT-PCR, a 25 μL reaction mixture droplet was prepared containing 12.5 μL of SYBR Premix Ex Taq II (2×), 1 μL each of forward and reverse primers (10 μM), 2 μL of cDNA solution, and 8.5 μL of ddH_2O. The amplification conditions are as follows: 95 °C for 30 s, followed by 40 cycles at 95 °C for 5 s, and 60 °C for 30 s. The expression levels of miRNA-155 were normalized using the endogenous reference gene U6, while quantification of fold change in miRNA-155 expression between experimental and control groups was performed using the $2^{-\Delta\Delta C_t}$ method.[1] qRT-PCR analysis was performed in triplicate for each sample, and the primer sequences utilized were documented in **Table S1**.

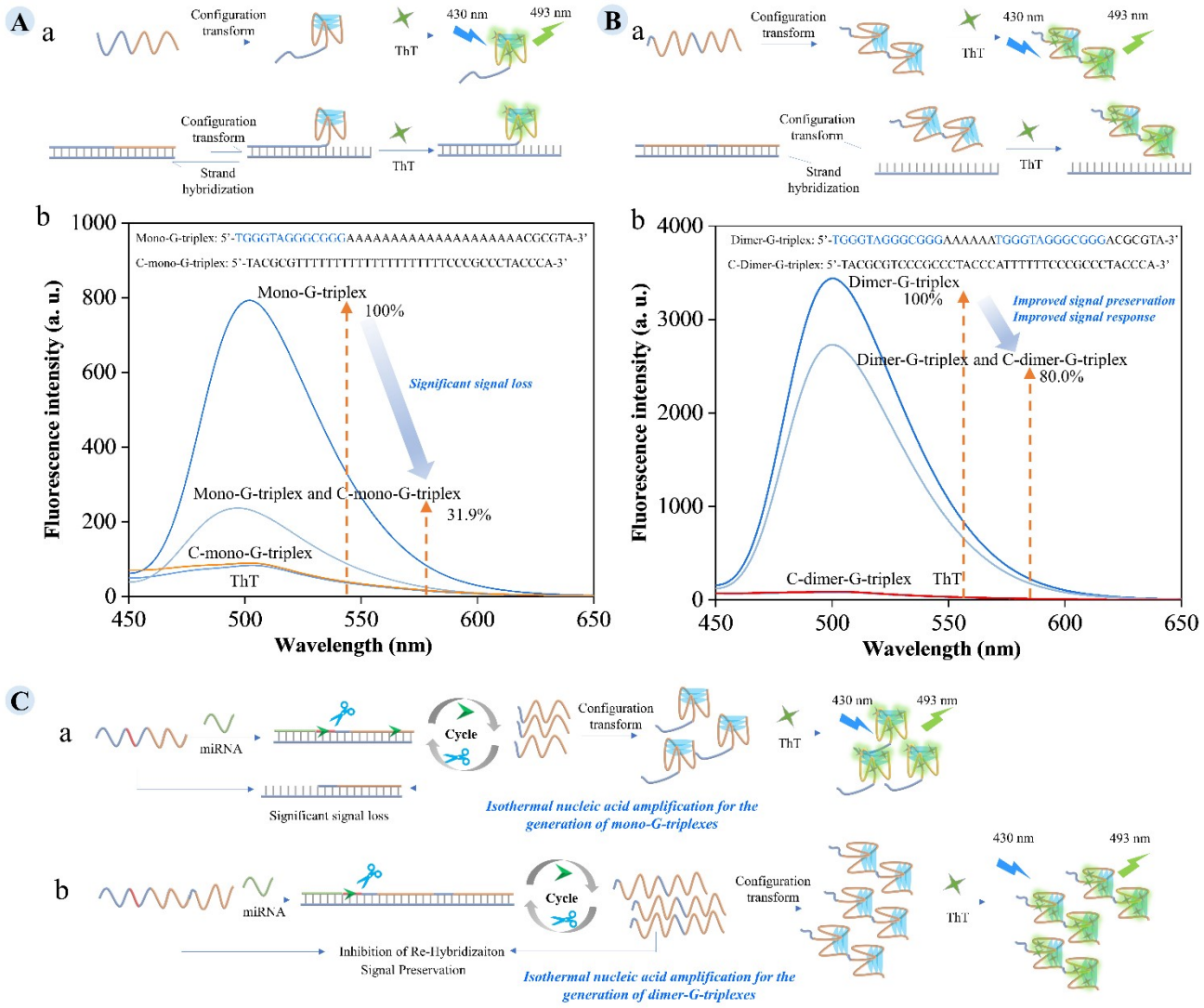

Figure S1. (A) Theoretical analysis and experimental demonstration of the mono-G-triplex based signal loss. (B) Theoretical analysis and experimental demonstration of the dimer-G-triplex based minimize signal loss. (C) Hypothetical cases for miRNA detection based on the generation of mono-G-triplexes or dimer-G-triplexes to show the advantage of using dimer-G-triplex as the signal transducer. Experimental conditions: [Mono-G-triplex] = [Dimer-G-triplex] = 125 nM, [C-mono-G-triplex] = [C-dimer-G-triplex] = 250 nM, [ThT] = 6 μM.

Theoretical analysis and experimental demonstration of signal retention. Mono-G-triplex and dimer-G-triplex are artificially designed functional oligonucleotide containing one and two G-triplex motifs, respectively. The sequences of C-mono-G-triplex and C-dimer-G-triplex are completely

complementary to mono-G-triplex and dimer-G-triplex, respectively. Panel a in **Figure S1A** illustrates that the configuration of mono-G-triplex is influenced by strong pairing forces between the remaining base portions connected to it and the parent strand. As a result, the mono-G-triplex is more prone to re-hybridize with the parent chain, impeding its binding with the signal reporting molecule ThT and resulting in significant loss of signal. The theoretical analysis is confirmed by the change observed in the fluorescence spectral curve in panel b of **Figure S1A**. The addition of abundant C-mono-G-triplex greatly reduced the fluorescence signal intensity compared to only mono-G-triplex binding to ThT (only 31.9% remained). In contrast, using dimer-G-triplex as the signal reporting unit in the amplification process, rather than the mono-G-triplex, would decrease complementarity between bases outside the G-triplex and the parent strand (Panel a of **Figure S1B**). This contributes to the maintenance of the G-triplex configuration, resulting in enhanced signal response and ensuring exceptional signal preservation. Experimental results from panel b in **Figure S1B** confirm that this strategy interaction between the dimer-G-triplex and ThT improves the signal response, preserving signal strength by 80.0%. To clarify the advantage of using dimer-G-triplex as the signal transducer, we hypothetical cases for miRNA detection based on the generation of mono-G-triplexes or dimer-G-triplexes. In panel a of **Figure S1C**, the miRNA triggers isothermal nucleic acid amplification through the coordinated action of Klenow polymerase and Nt.BbvCI endonuclease. However, the re-hybridization of the generation of mono-G-triplexes with its parent strand results in a reversal of configurational transformation, resulting in significant signal loss. In panel b, using dimer-G-triplexes as the signal reporting unit inhibits re-hybridization between it and the parent strand, thereby preserving the signal and improving the signal response.

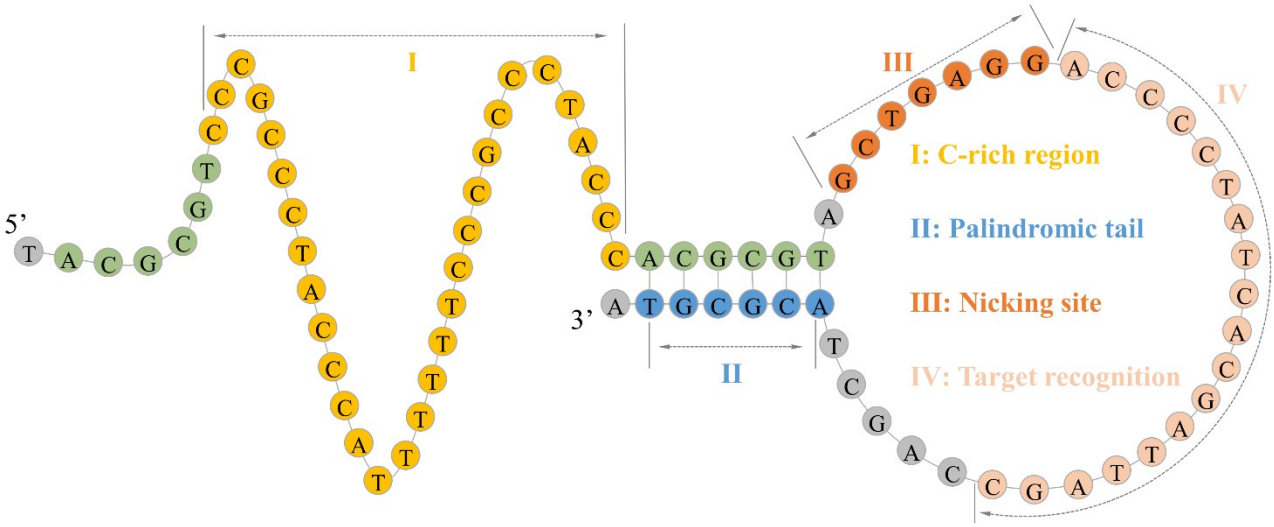

Figure S2. Detailed structure and function analysis of APHP.

Structure and function of APHP. In terms of functional analysis, as shown in **Figure S2**, the target complementary region is responsible for identifying the target miRNA, the recognition sequence of Nt.BbvCI is utilized to form the cleavage site, and the C-rich region is employed to generate a dimer-G-triplex with remarkable ability for signal output. The two identical segments play a crucial role in facilitating the cleavage products to interact with individual APHPs for the construction of Mode-I amplification. Simultaneously, the palindromic tail serves as a key element, enabling intermolecular interactions between different APHPs for the construction of Mode-II amplification.

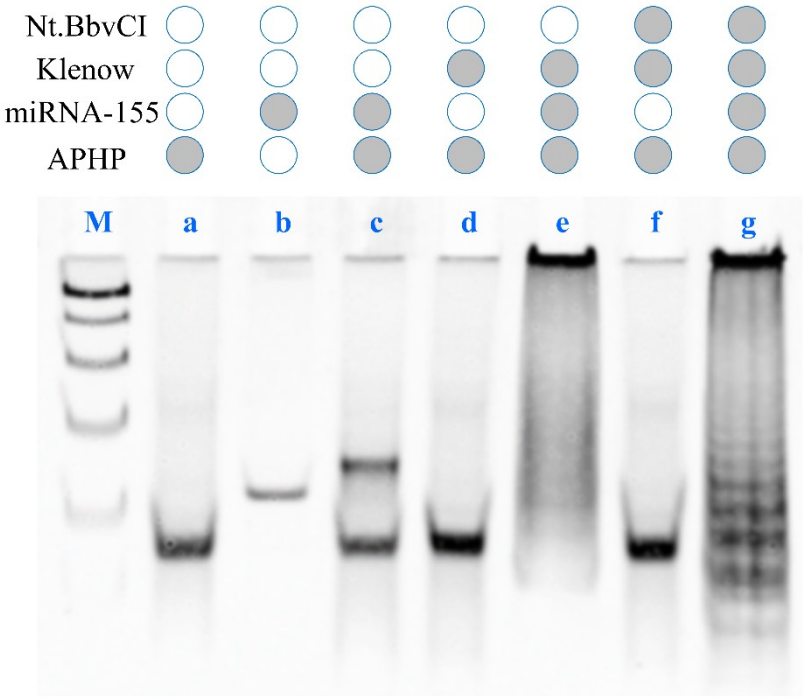

Figure S3. Photographed image of the (a) APHP, (b) miRNA-155, (c) APHP + miRNA-155, (d) APHP + Klenow, (e) APHP + miRNA-155 + Klenow, (f) APHP + Klenow + Nt.BbvCI, and (g) APHP + miRNA-155 + Klenow + Nt.BbvCI. "M" denotes the DNA marker. Experimental conditions: [APHP] = 50 nM, [miRNA-155] = 50 nM, [Klenow] = 25 U/mL, [Nt.BbvCI] = 50 U/mL.

Feasibility characterization by gel electrophoresis. In **Figure S3**, lanes a and b showcase representative bands of APHP and miRNA-155, respectively. Lane c displays a mixture of APHP and miRNA-155, where the appearance of a new band with delayed migration compared to APHP and miRNA-155 indicates successful hybridization between the two. Lane d illustrates the band of mixed APHP and Klenow polymerase. The sole presence of the APHP band suggests the stable configuration of APHP in the absence of the target stimulus. However, upon the addition of target miRNA-155 in lane e, a new band appears, blocked in the loading groove. This band represents the formation of the dimer-APHP/extended miRNA complex, attributed to palindrome tail base intermolecular pairing and replication. Lane f displays the results of APHP co-incubated with Klenow polymerase and Nt.BbvCI, resembling the outcomes in lanes a and d. This comparison suggests that the secondary structure of

APHP is well-designed to tightly lock its palindrome structure, preventing background amplification and signal leakage. In contrast, when encountering target miRNA, several bands with lower molecular weights appear in lane g, indicating successful nicking of the polymerization products. Considering the consistency among lanes a, d, and e, and the varied trend in lanes c, e, and g, we can confidently affirm the feasibility of our DMI-SDA for miRNA-155 analysis.

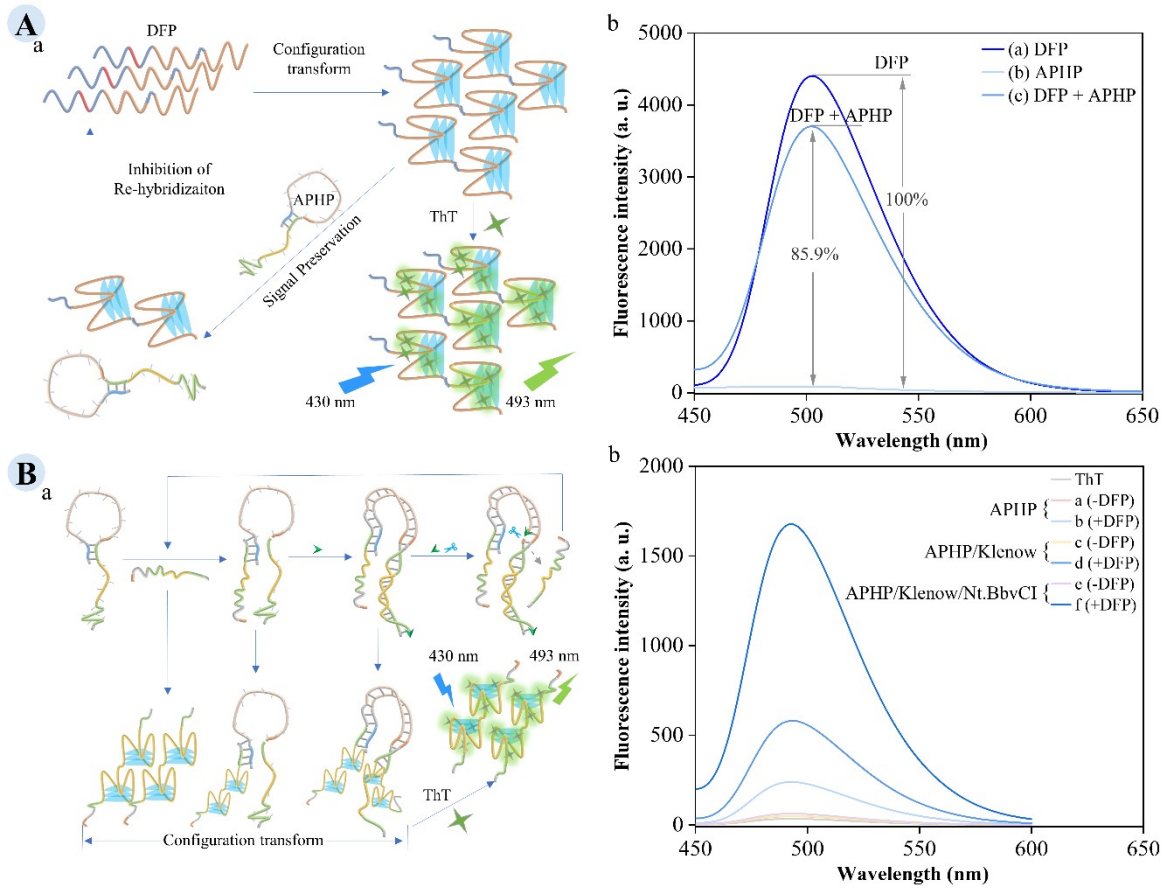

Figure S4. (A) Illustration of the interaction of DFP with APHP or ThT and typical fluorescence of the (a) DFP, (b) APHP, and (c) DFP mixed with APHP after binding with ThT. Experimental conditions: [DFP] = 125 nM, [APHP] = 250 nM, [ThT] = 6 μM. (B) Illustration of the reusability of APHP in DMI-SDA and fluorescent responses of the species containing (a) APHP, (b) APHP + DFP, (c) APHP + Klenow, (d) APHP + DFP + Klenow, (e) APHP + Klenow + Nt.BbvCI and (f) APHP + DFP + Klenow + Nt.BbvCI after binding with ThT. Experimental conditions: [APHP] = 50 nM, [DFP] = 50 nM, [Klenow] = 25 U/mL, [Nt.BbvCI] = 50 U/mL, [ThT] = 1 μM.

Signal preservation ability and repeated use of DPF demonstrations. According to the working principle, the DFP acts as a vital intermedium to indirectly regulate the DMI-SDA. To verify if it was functionalized as expected, we artificially synthesized DFP with sequences based on the reaction mechanism and then employed it to react with the APHP under different conditions. As illustrated in panel A of **Figure S4A**, DFP can form a dimer-G-triplex structure due to the presence of two lengthy

C-rich regions. By effectively avoiding the re-hybridization of DFP and APHP, this structure successfully maintains the signal integrity. Plane b in **Figure S4A** illustrates the enhanced fluorescence intensity resulting from the mixture of DFP and ThT (lane a). In the presence of APHP alone, there was no significant increase in fluorescence intensity observed upon mixing with ThT (lane b). The presence of APHP slightly reduces the fluorescence intensity, indicating that the dimer G-triplex formed by DFP has a high affinity for recognizing ThT instead of reassociating with APHP. This ensures the emission of greatly enhanced fluorescence and minimizes signal loss, enabling robust detection of the target miRNA (lane c). As validated caused by the mixture of DFP and APHP [$(F - F_0)/(F_t - F_0)$] were calculated to be 85.9%. F_t, F, and F_0 represent the peak fluorescence values of DFP, DFP + APHP, and APHP, respectively.

To determine whether DFP exhibits recycling characteristics, such as signal amplification potential, we performed further confirmatory experiments. As depicted in panel a of **Figure S4B**, the palindromic tail of DFP can undergo hybridization with APHP, leading to iterative strand cleavage, polymerization, and displacement facilitated by Kelnow and Nt.BbvCI enzymes, thereby yielding amplified quantities of DFP. As shown in plane b of **Figure S4B**, incubation of DFP with MF-HP (line b) resulted in signal enhancement compared to single APHP (line a). This can be attributed to the presence of dimer-G-triplex within DFP. When Klenow was combined with DFP (line d), there was only a slight increase in fluorescence response compared to using Klenow alone (line c). It is evident that the presence of both DFP and Klenow, APHP-locked palindromic tails are released. These released palindromic fragments can hybridize with each other and undergo polymerase shift, resulting in the generation of a set of sequences containing DFP. Similarly, the observed changes in signal for APHP/Klenow/Nt.BbvCI (line e) were consistent with those for APHP (line a) and APHP/Klenow

(line c). The addition of Nt. BbvCI and Klenow (line f) resulted in a significantly higher maximum fluorescence signal compared to the APHP/Klenow/DFP mixture (line d). These results demonstrate the recyclability of DFP effectively.

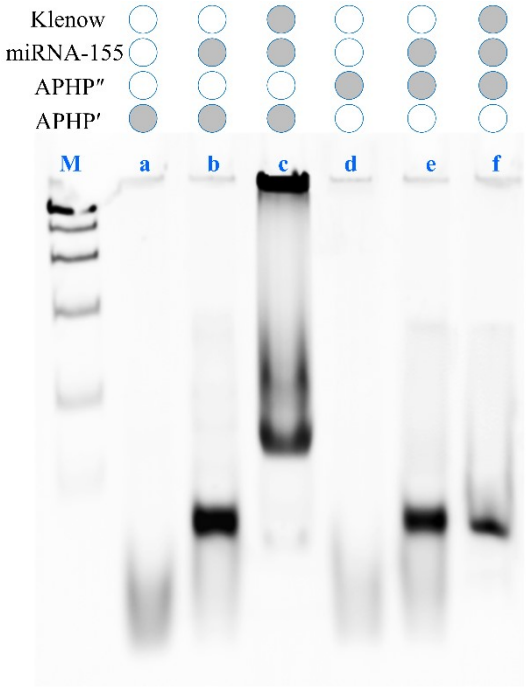

Figure S5. Demonstration of palindromic tail-based reverse reading using a 12% Native-PAGE. Lane a: APHP', lane b: APHP'/miRNA-155, lane c: APHP'/miRNA-155/Klenow, lane d: APHP", lane e: APHP"/miRNA-155, and lane f: APHP"/miRNA-155/Klenow. Experimental conditions: [APHP′] = [APHP″] = 50 nM, [miRNA-155] = 50 nM, and [Klenow] = 25 U/mL.

Palindromic tail based reverse reading demonstration. To validate the functionality of the inverse reading function of the palindromic tail, we synthesized separate APHP′ and APHP″ sequences based on the currently used APHP. APHP′ retains the stem and loop sequence of APHP, while APHP″ has an identical sequence to APHP′, except for a substitution of A base with T base at its 3' end. This design of APHP′ ensures the simplification of APHP's structure but maintains the palindromic tail, while the design of APHP″ eliminates the palindromic tail. Both APHP' and APHP″ were then used to react with the target miRNA and Klenow and characterized by Native-PAGE. In **Figure S5**, lanes a and d show the observed bands of APHP' and APHP″, respectively. In the presence of miRNA-155, either APHP' or APHP″ forms a hybrid complex with miRNA-155, resulting in the appearance of a new band in lane b or lane e, respectively. Their new bands are located at the same potion. However,

when encountered with Klenow, a significant difference was observed between APHP'/miRNA-155 (lane c) and APHP″/miRNA-155 (lane f). For the APHP'/miRNA-155 duplex, a new band with significantly retarded mobility was observed after incubation with Klenow polymerase. In contrast, no other bands were observed, even when involved with Klenow polymerase for the APHP″/miRNA-155 duplex. Considering that the main difference lies in the presence or absence of the palindromic tail between APHP' and APHP″, the different gel results in lanes c and f confirm the reverse reading ability of the palindromic structure.

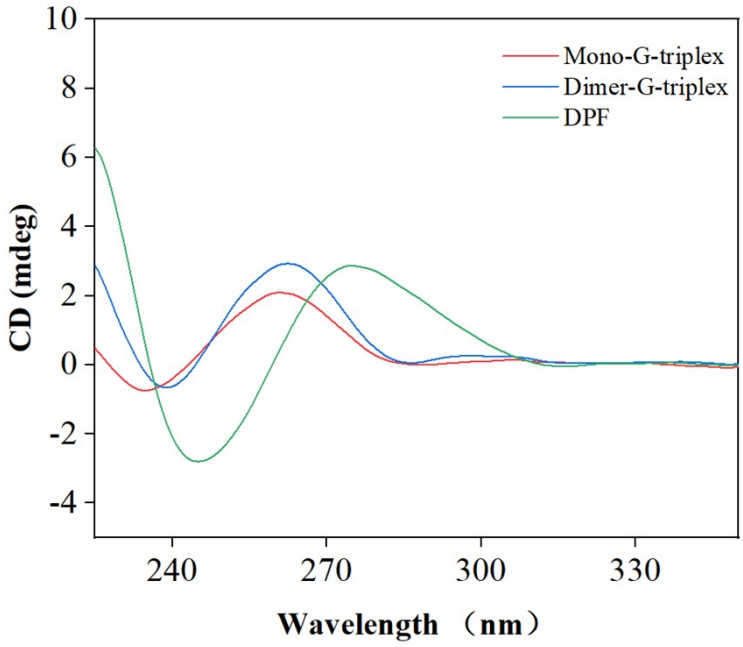

Figure S6. Circular dichroism (CD) measurements of mono-G-triplex, dimer-G-triplex, and the amplified product of DPF in Tris-buffer.

Characterization of G-triplex Structure: To assess the formation of the anticipated G-triplex structure in the generated G-rich sequence, circular dichroism (CD) measurements were employed to elucidate the secondary structure of sequences corresponding to mono-G-triplex, dimer-G-triplex, and the amplified product of DPF in Tris-buffer. As depicted in **Figure S6**, both mono-G-triplex and dimer-G-triplex exhibited a robust positive peak around 265 nm and a negative peak at 240 nm, consistent with previously reported G-triplex structure findings.[2, 3] Similarly, notwithstanding a shift in peak values due to sequences beyond the G-rich region, the CD spectra of the amplified DPF product also demonstrated a similar profile, confirming the formation of the G-triplex structure.

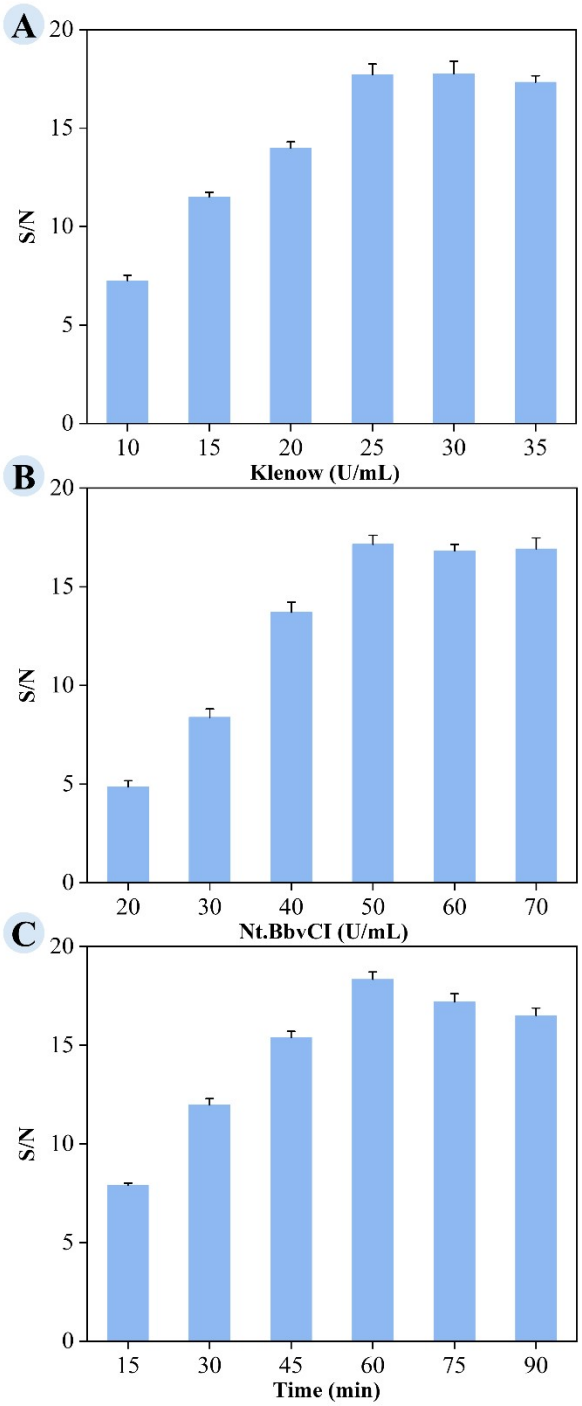

Figure S7. Optimization of experimental conditions to show the effects of (A) Klenow amount, (B) Nt.BbvCI amount, and (C) reaction time on the DMI-SDA assay performance for miRNA-155 detection. Fluorescent values are recorded at 493 nm. Error bars are from at least three independent measurements. Experimental condition: (A) [APHP] = 50 nM, [miRNA-155] = 50 nM, [Nt.BbvCI] = 50 U/mL, T = 60 min, [ThT] = 1 μM. (B) [APHP] = 50 nM, [miRNA-155] = 50 nM, [Klenow] = 25 U/mL, T = 60 min, [ThT] = 1 μM. (C) [APHP] = 50 nM, [miRNA-155] = 50 nM, [Klenow] = 25 U/mL, [Nt.BbvCI] = 50 U/mL, [ThT] = 1 μM.

Optimization of experimental conditions. To enhance assay performance, we systematically optimized key experimental parameters, specifically the amounts of Klenow and Nt.BbvCI, as well as the reaction time. They can significantly impact the enzyme-based amplification. The concentration of APHP and ThT were maintained at 50 nM and 1 μM, respectively, throughout the optimization process. Initially, the dependence of fluorescent intensity on the amount of Klenow was investigated in **Figure S7A**. The S/N value was increased with the increase of the Klenow from 10 to 25 U/mL and then leveled off. Consequently, 25 U/mL was identified as the optimal Klenow amount for subsequent experiments. **Figure S7B** presents the optimization results for Nt.BbvCI endonuclease, revealing a similar trend to that observed for Klenow in **Figure S7A**. The optimal amount of Nt.BbvCI endonuclease was thus determined to be 50 U/mL. Additionally, the impact of isothermal reaction time on the peak fluorescence intensity was assessed in **Figure S7C**. The results demonstrated a continual increase in the S/N responses with the extension of reaction time from 15 to 60 min. However, owing to the increase of the background signal, the S/N decreased beyond 60 min. Consequently, the reaction time was set at 60 min for the experiments. These optimized conditions collectively contribute to the improved performance of the DMI-SDA assay for miRNA-155 detection.

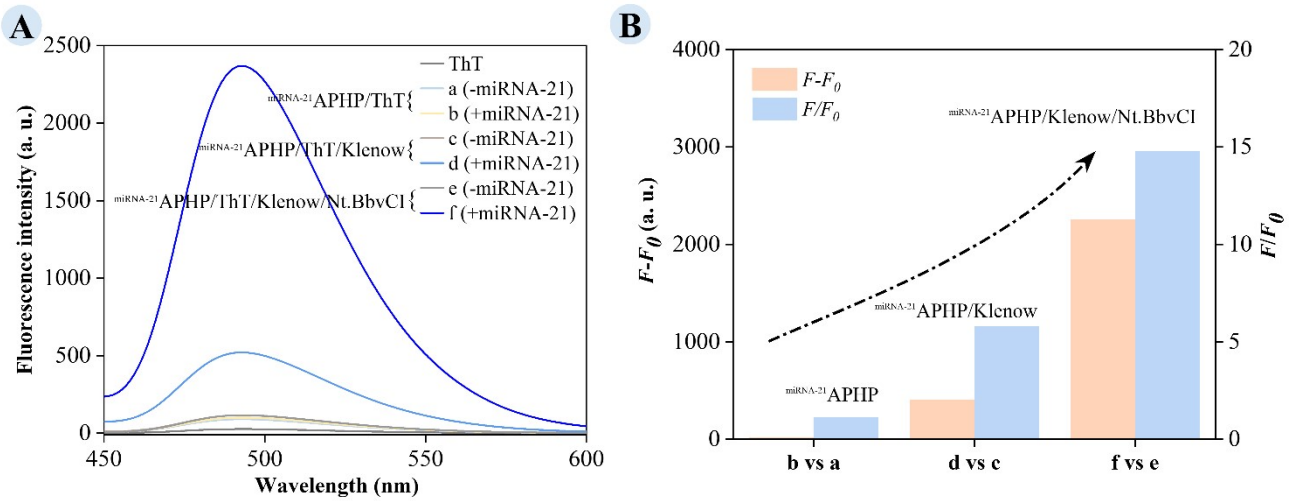

Figure S8. (A) Typical fluorescence intensities obtained from the species of (a) $^{miRNA\text{-}21}$APHP, (b) $^{miRNA\text{-}21}$APHP + miRNA-21, (c) $^{miRNA\text{-}21}$APHP + Klenow, (d) $^{miRNA\text{-}21}$APHP + miRNA-21 + Klenow, (e) $^{miRNA\text{-}21}$APHP + Klenow + Nt.BbvCI, (f) $^{miRNA\text{-}21}$APHP + miRNA-21 + Klenow + Nt.BbvCI. (B) Comparison of fluorescence increase ($F - F_0$) and signal-to-noise ratio (F/F_0) of line b vs a, line d vs c and line f vs e. Experimental conditions: [$^{miRNA\text{-}21}$APHP] = 50 nM, [miRNA-21] = 50 nM, [Klenow] = 25 U/mL, [Nt.BbvCI] = 50 U/mL, [ThT] = 1 μM.

Verification of application universality of DMI-SDA for miRNA analysis. The newly developed DMI-SDA, based on APHP, was initially designed for miRNA-155 analysis. To assess the universality of this approach, we extended its application to the detection of another miRNA of interest, specifically miRNA-21. A miRNA-21-responsive analog, $^{miRNA\text{-}21}$APHP, was designed similarly to APHP and utilized for miRNA-21 detection following the same experimental procedures employed for miRNA-155. As depicted in **Figure S8A**, the presence of miRNA-21 (line b) did not induce the unfolding of $^{miRNA\text{-}21}$APHP (line a) for signal reporting. The addition of Klenow significantly enhanced the signal of $^{miRNA\text{-}21}$APHP/miRNA-21 (line d vs c), while the co-addition of Klenow and Nt.BbvCI (line f vs e) resulted in maximal signal amplification for miRNA-21 detection. In **Figure S8B**, the fluorescence increase ($F - F_0$) and signal-to-noise ratio (F/F_0) values for line b vs a, line d vs c, and line f vs e are

presented. It is evident that the use of $^{miRNA\text{-}21}$APHP for miRNA-21 detection, with the involvement of Klenow or the combination of Klenow/Nt.BbvCI, exhibits signal differences (line b vs a, line d vs c, and line f vs e) consistent with the data trends observed in **Figure 1** for miRNA-155 detection. These results robustly affirm the broad applicability of the newly proposed DMI-SDA protocol, exhibiting its effectiveness in miRNA analysis beyond miRNA-155.

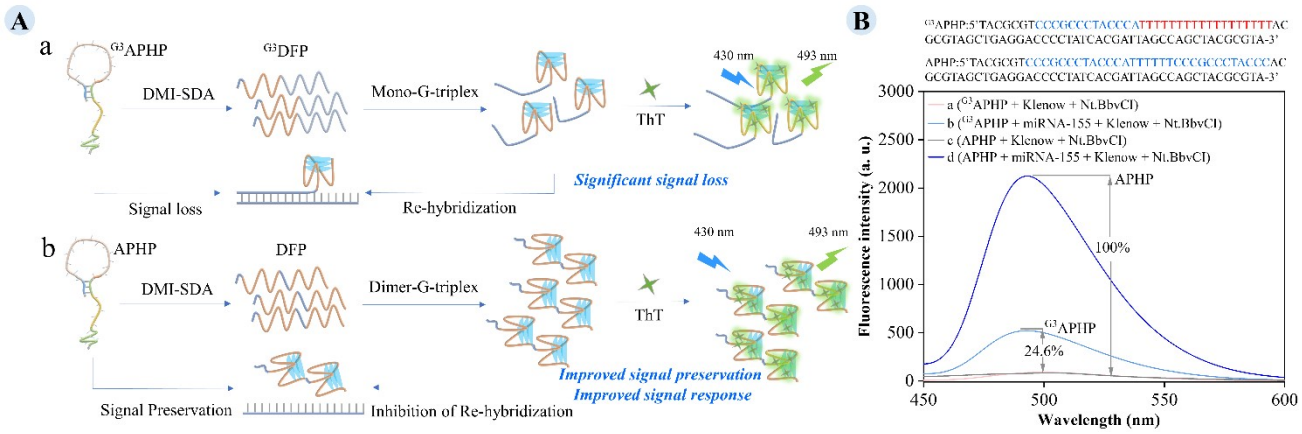

Figure S9. (A) Theoretical analysis of miRNA detection based on ^{G3}APHP and APHP is conducted to demonstrate the superiority of utilizing APHP as the signal transducer. (B) Fluorescent responses of ^{G3}APHP and APHP based sensing systems before and after added with miRNA-155, respectively. (a) ^{G3}APHP + Klenow + Nt.BbvCI, (b) ^{G3}APHP + miRNA-155 + Klenow + Nt.BbvCI, (c) APHP + Klenow + Nt.BbvCI, and (d) APHP + miRNA-155 + Klenow + Nt.BbvCI. Experimental conditions: [APHP] = 50 nM, [^{G3}APHP] = 50 nM, [miRNA-21] = 50 nM, [Klenow] = 25 U/mL, [Nt.BbvCI] = 50 U/mL, [ThT] = 1 μM.

Comparison of ^{G3}APHP based DMI-SDA and APHP based DMI-SDA in fluorescent signaling. Panel a in **Figure S9A** illustrates that the formation of ^{G3}DFP from ^{G3}APHP is influenced by strong pairing forces between its remaining base portions and the parent strand, resulting in a significant signal loss. In contrast, utilizing DFP as a signal reporting unit during amplification reduces complementarity with the parent strand, thereby enhancing both signal response and retention (see Panel b of **Figure S9A**). As described earlier, the APHP-based DMI-SDA is capable of generating dimer-G-triplex structures, which exhibit strong fluorescence upon binding with ThT. In this context, we have introduced a variant of APHP, termed ^{G3}APHP, specifically designed to produce mono-G-triplex during DMI-SDA. As illustrated in **Figure S9B**, the background signals of both ^{G3}APHP-based DMI-SDA and APHP-based DMI-SDA are negligible in the absence of the target. However, upon the

introduction of an equal amount of target miRNA, the signal generated by APHP-based DMI-SDA significantly surpasses that produced by ^{G3}APHP-based DMI-SDA. This observation demonstrates the superiority of the current APHP-based DMI-SDA, attributed to the minimal signal loss associated with the formation of dimer-G-triplex compared to the produced mono-G-triplex. Furthermore, the presence of more G-triplex units in the dimer-G-triplex contributes to its enhanced performance. Collectively, these effects highlight the advantages of dimer-G-triplex in this amplification strategy.

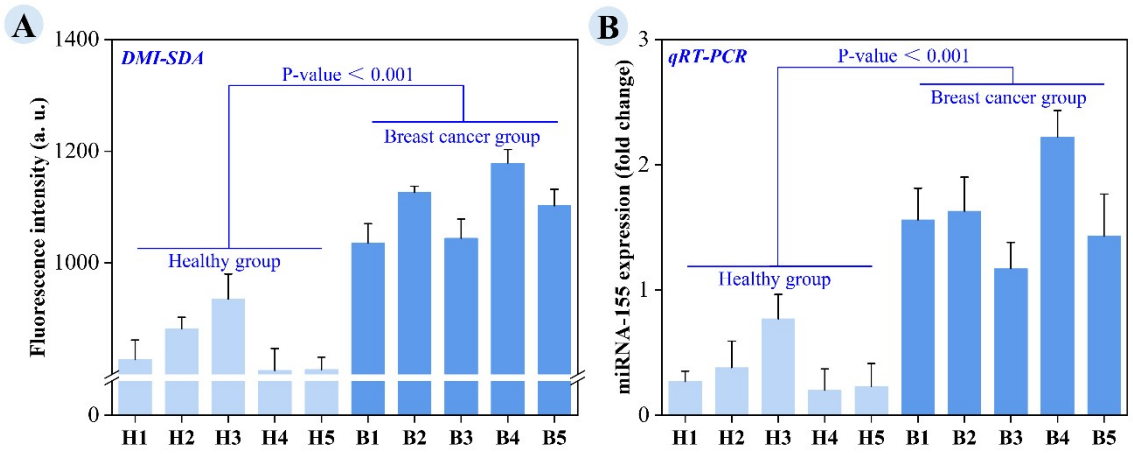

Figure S10. Determination of miRNA-155 in human blood samples by DMI-SDA (A) and standard qRT-PCR (B), respectively. Error bars are from three repetitive tests.

Practicability verification. To validate the practicability of the DMI-SDA, we conducted assays using real human blood samples and extracted miRNAs using a commercial kit. **Figure S10A** illustrates the fluorescence response intensity for detecting miRNA-155 in real human blood samples. Obviously, breast cancer patients (B1-B5) exhibited a substantial increase in fluorescence intensity compared to healthy donors (H1-H5). These findings are in accordance with prior reports indicating the upregulation of miRNA-155 in breast cancer patients. Concurrently, we employed standard quantitative real-time PCR (qRT-PCR) to assess the accuracy of our DMI-SDA by examining the same clinical samples. **Figure S10B** depicts the qRT-PCR results, revealing a higher miRNA-155 expression level in breast cancer patients compared to healthy individuals. Moreover, the individual miRNA content obtained by qRT-PCR also exhibited a consistent trend with the results obtained by DMI-SDA. The consistency between the qRT-PCR results and the DMI-SDA results validates the availability of our method in practical applications. Recovery tests in **Table S3** also confirms the potential practicability.

Table S1. Oligonucleotides used in the current study

Items	Sequences (5' to 3' order)
APHP	TACGCGTCCCGCCCTACCCATTTTTTCCCGCCCTACCCacgc gtagctgAGGACCCCTATCACGATTAGCcagctacgcgtA
APHP′	acgcgtagctgAGGACCCCTATCACGATTAGCcagctacgcgtA
APHP″	acgcgtagctgAGGACCCCTATCACGATTAGCcagctacgcgtT
$^{miRNA\text{-}21}$APHP	TACGCGTCCCGCCCTACCCATTTTTTCCCGCCCTACCCacgc gtagctgAGGTCAACATCAGTCTGATAcagctacgcgtA
^{G3}APHP	TACGCGTCCCGCCCTACCCATTTTTTTTTTTTTTTTTacgcgt agctgAGGACCCCTATCACGATTAGCcagctacgcgtA
DPF	TCAGCTACGCGTGGGTAGGGCGGGAAAAAATGGGTAGGG CGGGACGCGTA
Mono-G-triplex	TGGGTAGGGCGGGaaaaaaaaaaaaaaaaaaaACGCGTA
C-mono-G-triplex	TACGCGTttttttttttttttttttCCCGCCCTACCCa
Dimer-G-triplex	TGGGTAGGGCGGGaaaaaaTGGGTAGGGCGGGACGCGTA
C-dimer-G-triplex	TACGCGTCCCGCCCTACCCAtttttCCCGCCCTACCCa
miRNA-155	UUAAUGCUAAUCGUGAUGGGGT
MT1	UUAAUGCUAAUGGUGAUAGGGGU
MT2	UUAUUGCUAAUCGUGAUAGCGGU
MT3	UUAUUGCUAAUGGUGAUAGCGGU
miRNA-10b	UACCCUGUAGAACCGAAUUUGUG
let-7d	AGAGGUAGUAGGUUGCAUAGUU
miRNA-141	UAACACUGUCUGGUAAAGAUGG
miRNA-200b	UAAUACUGCCUGGUAAUGAUGA
miRNA-21	UAGCUUAUCAGACUGAUGUUGA
RT miR-155 stem-loop	GAAAGAAGGCGAGGAGCAGATCGAGGAAGAAGACGGAA GAATGTGCGTCTCGCCTTCTTTCACCCCTAT
RT-U6	CGCTTCACGAATTTGCGTGTCA
miRNA-155 forward primer	CTCAGACTCGGTTAATGCTAATCGTGATAGG
miRNA-155 reverse primer	GCTGTGGCAGTGGAAGCGTGATTTATT
U6 RNA forward primer	CTCGCTTCGGCAGCACA
U6 RNA reverse primer	AACGCTTCACGAATTTGCGT

Note: Underlined bases in APHP or ^{G3}APHP is complementary with the underlined bases in miRNA-155. The highlighted bases in APHP or ^{G3}APHP are complementary regions of the DNA sequence that form mono-G-triplex or dimer-G-triplex. The red colored bases of APHP, ^{G3}APHP and $^{miRNA\text{-}21}$APHP represent half of the Nt.BbvCI recognition site. The lowercase bases in APHP or ^{G3}APHP represent the complementary regions that facilitate the formation of a hairpin structure. Compared with target

miRNA-155, the mutant bases of non-targets (MT1, MT2, MT3) are shown in shadow. Notably, we intentionally selected six consecutive "A" bases between the two mono-G-triplex motifs based on the rationale that "A" has the minimal impact on "G" bases. Other bases could potentially interfere with the formation of a stable G-triplex structure for instance. For instance, T and "G" can establish weak hydrogen bonds, while "C" and "G" can form strong hydrogen bonds. Additionally, "G"-"G" interactions involve π-π stacking. Considering the minimal impact of "A" on guanine, we chose "A" bases as the linker between the mono-G-triplex motifs.

Table S2. Comparison of assay performance of reported analytical methods with the current DMI-SDA for miRNA detection.

Methods	LOD	Linear range	Orders of amplification	Ref.
Chemoreceptive biosensor based on layered graphene oxide/graphene composite	14.6 pM	10 pM to 100 nM	5	[4]
Dual ferrocene-labeled DNA hairpin based on Mg^{2+}-dependent DNAzyme-cleavage cycling	1.8 fM	10 fM to 100 pM	5	[5]
Target recycling and palindrome-mediated strand displacement amplification	50 pM	50 pM to 300 nM	5	[6]
DNA-AgNCs based on fluorescent resonance energy transfer	4 pM	20 pM to 100 nM	5	[7]
Duplex-specific nuclease-assisted CRISPR-Cas12a strategy	2.4 pM	10 pM to 100 nM	5	[8]
Target-triggered hybridization chain reaction	1.92 fM	5 fM to 10 pM	5	[9]
Three-dimensional bipedal DNA walkers based on exponential amplification reaction	5.2 fM	10 fM to 5 nM	6	[10]
Mismatched catalytic hairpin probe based on electrochemical detection	1.1 pM	5 fM to 100 pM	6	8
DMI-SDA	1.06 fM	10 fM to 1 nM	6	This study

Table S3. Recovery Rates of miRNA-155 from Spiked Blood Samples (n = 3).

Samples	Spiked	Found	Recovery (%)	RSD (%)
1	10 pM	9.52 pM	95.2	1.79
2	1 nM	0.96 nM	96.1	2.05
3	100 nM	97.8 nM	97.8	1.58

References

1. K. J. Livak and T. D. Schmittgen, *Methods*, 2001, **25**, 402-408.
2. Hui, Zhou, Zhi-Fang, Wu, Qian-Jin, Han, Hong-Mei, Zhong, Jun-Bin and Peng, *Anal. Chem.*, 2018, **90**, 3220-3226.
3. Q. Zhang, T. Yang, G. Zheng, H. Gao, C. Yan, X. Zheng, X. Zhou and Y. Shao, *Analyst*, 2020, **145**, 4254-4259.
4. C. H. Huang, T. T. Huang, C. H. Chiang, W. T. Huang and Y. T. Lin, *Biosens Bioelectron*, 2020, **164**, 112320.
5. X. Lin, J. Jiang, J. Wang, J. Xia, R. Wang and G. Diao, *Sens. Actuators, B*, 2021, **333**, 129556.
6. H. Xu, B. Wu, J. Wang, H. Cao, J. Yang, K. Hao, S. Chen, S. Ye and Z. Shen, *Talanta*, 2020, **215**, 120897.
7. V. Nasirian, M. Shamsipur, F. Molaabasi, K. Mansouri, M. Sarparast, V. Salim, A. Barati and S. Kashanian, *Sens. Actuators, B*, 2020, **308**, 127673.
8. S. Gong, J. Li, W. Pan, N. Li and B. Tang, *Anal. Chem.*, 2021, **93**, 10719-10726.
9. Y. Wang, H. Feng, K. Huang, J. Quan, F. Yu, X. Liu, H. Jiang and X. Wang, *Biosens. Bioelectron.*, 2022, **215**, 114572.
10. L. Yang, J. Fang, J. J. Li, X. Y. Ou, L. Zhang, Y. F. Wang, Z. Weng and G. M. Xie, *Anal. Chim. Acta*, 2021, **1143**, 157-165.